Journal of Sound and Vibration 536 (2022) 117100

Contents lists available at ScienceDirect

Journal of Sound and Vibration

journal homepage: www.elsevier.com/locate/jsvi

Linear and nonlinear modelling of far-field propagation of broadband shock-associated noise

S.A. Karabasov [a,1], A.P. Markesteijn [a,2], V. Gryazev [a,*,2], A. Kalyan [a,3], S.N. Gurbatov [b,4], I.Yu. Demin [b,5], A.A. Lisin [b,6], A.V. Tyurina [b,6]

[a] *Queen Mary, University of London, London E1 4NS, United Kingdom*
[b] *Lobachevsky State University, 23 Gagarin Av., Nizhny Novgorod, 603950, Russia*

ARTICLE INFO

Keywords:
Broadband shock-associated noise
Linear and nonlinear modelling

ABSTRACT

A triple-scale computational model is implemented to simulate noise generated by a supersonic under-expanded screeching jet corresponding to the LTRAC (Laboratory for Turbulence Research in Aerospace and Combustion) experiment at different distances from the source. The investigation is focused on the broadband-associated noise, which is a prominent feature of the acoustic field of the LTRAC jet. In the jet near-field, the compressible Navier–Stokes equations are solved using the high-resolution CABARET Large Eddy Simulation (LES) method accelerated on Graphics Processing Units. The LES solution is substituted in the Ffowcs Williams–Hawkings (FW–H) model to obtain the noise solution in the acoustic mid field at 20 initial jet diameters from the jet nozzle exit. The mid-field acoustic solution is used as the input for the spherical generalised Burgers' equation. The general form of Burgers' equation is solved numerically in the frequency domain for a wide range of observer distances up to 18 million initial jet diameters, where viscous dissipation fully dominates for most frequencies. To answer the question if the nonlinear acoustic wave propagation effects for the LTRAC jet are important, the nonlinear and linear solutions of Burgers' equation are compared.

1. Introduction

The importance of nonlinear effects for propagation of high intensity jet noise has been a subject of active investigation since the first Concorde flight [1] where the flyover measurements showed an anomalous amplification of the high-frequency part of the noise spectrum in comparison with the linear acoustic models. For example, the propagation of high-intensity aircraft noise was described in detail in [2]. More recent studies, which investigate the jet engine noise at full power show that nonlinear distortions of the acoustic spectra have a significant impact on the noise field [3,4]. In addition, the nonlinear wave reflection effects are important in the acoustic near-field for ground-based measurements [5]. In parallel to the experimental efforts, the nonlinear jet noise propagation, which involves the nonlinear wave steepening effects and shock coalescence, has been a subject of several

* Corresponding author.
E-mail address: v.gryazev@qmul.ac.uk (V. Gryazev).
[1] Professor, School of Engineering and Material Sciences.
[2] Post-Doctoral Researcher, School of Engineering and Material Sciences.
[3] Visiting Researcher, School of Engineering and Material Sciences.
[4] Professor, Division of Physical Acoustics, Department of Radio Physics.
[5] Associate Professor, Division of Physical Acoustics, Department of Radio Physics.
[6] Ph.D. Student, Division of Physical Acoustics, Department of Radio Physics.

https://doi.org/10.1016/j.jsv.2022.117100
Received 21 September 2021; Received in revised form 6 April 2022; Accepted 5 June 2022
Available online 11 June 2022

Nomenclature

D_j	Nozzle diameter
D_{ef}	Fully expanded jet diameter
E	Acoustic energy spectrum
M_{fe}	Fully expanded Mach number
R_0	Ratio between the initial radius and nonlinear distance
Re	Reynolds number based on the fully expanded jet diameter
Re_a	Acoustic Reynolds number
p_0	Stagnation pressure
p_∞	Ambient pressure
r_0	Initial radius: effective radius of the source
r_{nl}	Effective distance when nonlinear effects become important
r_l	Effective distance when dissipation effects become important
T_0	Stagnation temperature
T_∞	Ambient temperature
U_j	Jet velocity at the nozzle throat
ε	Ratio between nonlinear distance and linear distance

investigations [6–8]. In the acoustic far-field, such wave processes lead to the formation of noise spectra of the triangular shape, which is typical of the nonlinear acoustic processes such as wave-steepening effects [9,10].

On the other hand, the nonlinear propagation effect is not the only possible mechanism of formation of steep acoustic wave fronts. In particular, for laboratory-scale jets [4,11] the nonlinear propagation effects may only be important in the jet near field while the nonlinearity effect on the far-field propagation is negligible. For example, another mechanism responsible for the formation of steep acoustic waves in the far-field includes the shock interaction with the turbulent shear layers, the wave structures of which linearly transmitted to the far-field [12–15]. The geometrical propagation law, which is spherical further away from the jet flow, is another important factor determining the nonlinear wave steepening process. In the far-field, the nonlinear wave propagation competes with the linear atmospheric absorption effects. The interplay between the nonlinear and linear dissipation effects is expressed via the inverse acoustic Reynolds number (the Goldberg number), which is not only strongly dependent on the flow conditions such as the jet nozzle pressure and temperature ratio but also the effective distance from the jet [16].

In order to quantify the importance of nonlinear propagation effects on supersonic jet noise, several studies compared the solution of the linear and nonlinear acoustic propagation models for the same initial conditions. The existing models in the literature can be classed into two categories. The first category includes theoretical models, which employ semi-analytical solutions of the one-dimensional Burgers' equation and Navier–Stokes equations [7,17]. Such models are computationally efficient but cannot take into account the effect of high Reynolds-number turbulence and the distributed nature of supersonic jet noise sources. In comparison with these, the second category of models comprises the solution of the three-dimensional compressible Navier–Stokes equations including turbulence effects and extending the simulation domain to the far-field by combining the Navier–Stokes solution with the Euler solution away from the jet issuing from a low-aspect ratio nozzle [6,18,19]. The range of the far-field noise propagation distances considered with such methods is limited to a few hundred initial jet diameters, which may be insufficient to fully describe the nonlinear-linear propagation regimes including the linear dissipation region.

The present work is devoted to the modelling of far-field noise generated by a cold supersonic under-expanded jet flow in accordance with the conditions of the flow experiment conducted in the Laboratory for Turbulence Research in Aerospace and Combustion (LTRAC) Supersonic Jet Facility at Monash University [20]. The particular jet conditions correspond to the fastest LTRAC jet case, where the jet issues from a high area ratio nozzle at a Nozzle Pressure Ratio of 4.2 generating a Mach disk and notable shock cells in the entire jet including the shear layers due to mismatch between the pressure at the nozzle exit and the ambient pressure [21,22]. The interaction of turbulence with prominent shock cells, which form in the shear layer leads to strong Broadband Shock Associated Noise (BBSAN) especially notable for sideline observer angles. The peaks are primarily associated with the regions where these shock cells interact with the turbulent eddies in the shear layers. To model the far-field propagation of BBSAN of the LTRAC jet, a triple-scale model has been implemented using the domain decomposition approach. In the nonlinear jet flow region, the Navier–Stokes equations are solved in the framework of the Monotonically Integrated LES (MILES) approach starting from the nozzle exit where the conditions are prescribed from the LTRAC Particle Image Velocimetry (PIV) dataset. At the second step, the LES solution is combined with the penetrable formulation of the Ffowcs Williams–Hawkings (FW–H) method [23,24] to obtain the noise spectra predictions in the acoustic near-field at 20 nozzle diameters from the nozzle exit for a few observer angles representative of the strongest BBSAN. For these angles, the noise spectra include the characteristic BBSAN hump which is typical of nonlinear acoustic effects. In the previous publication [25], the LES solution together with the far-field noise predictions at a far-field microphone location was validated in comparison with the experiment and the results of the empirical sJet model [26,27], which is based on the scaling laws calibrated over a large database of NASA jets. In the current work, we combine the acoustic near-field predictions of the LES-FW–H model with the solution of the generalised Burgers' equation [28]. The pressure spectrum obtained from the FW–H solution at the peak BBSAN polar angle is converted to the velocity spectrum and then used as an input to generate realisations of the stochastic velocity signal in the frequency domain. For each realisation, the generated velocity signal is applied as a boundary condition for the Burgers' equation under the assumption of a spherically symmetric far-field acoustic propagation. Notably, because of the peak BBSAN levels used in the model, the spherical symmetry assumption leads to some overestimation of the BBSAN source in the Burgers' equation. The spherical generalised Burgers' equation is then solved numerically to propagate the solution to the far-field until the linear dissipation effect becomes dominant. The propagation modelling is performed with and without including the nonlinear acoustic term to evaluate the effect of nonlinearity on the far-field noise spectra using the same mid-field acoustic spectrum as the initial wave condition. This approach is in agreement with [29], where it was theoretically and experimentally shown that the field spectrum at the discontinuous stage has a universal structure which is determined by the probability distribution of the initial wave frequency.

Preliminary results of this work were reported in [30], and the current article presents results of the extended simulation and analysis.

2. Solution of the Burgers' model of nonlinear wave propagation in the spherical case

Generalised Burgers' equations describe long-range propagation of cylindrical and spherical waves emitted by the stochastic source such as the turbulence–shock wave interaction in an imperfectly expanded supersonic jet flow. An important problem in this field is to find the behaviour of the wave far from the emitting source for stochastic initial waveforms defined at some distance from the turbulent source. The key equation for propagation of nonlinear spherical waves in viscous media without dispersion is the general form of Burgers' equation [28],

$$\frac{\partial V}{\partial r} + \frac{V}{r} - \frac{\beta}{c^2} V \frac{\partial V}{\partial t} = \frac{b}{2c^3\rho} \frac{\partial^2 V}{\partial t^2}, \tag{1}$$

where $V(r,t)$ is the group velocity in the acoustic wave, c is the sound speed at the unperturbed far-field, ρ is the unperturbed far-field density, b is kinematic molecular diffusion coefficient, r is the radial distance from the source, β is the so-called nonlinearity parameter of the media, which for air is approximately equal to 0.5. After some re-arrangement, the governing Burgers' equation reduces to the canonical one-dimensional form,

$$\frac{\partial U}{\partial R} - U \frac{\partial U}{\partial \tau} = \varepsilon g(R) \frac{\partial^2 U}{\partial \tau^2}, \tag{2}$$

where several new dimensionless variables are introduced:

$$\begin{gathered} U = \frac{r}{r_0}\frac{V}{V_0}, \\ \tau = \omega_0 t, \quad x = \frac{r - r_0}{r_{nl}}, \quad R_0 = \frac{r_0}{r_{nl}}, \quad R = R_0 \ln\left(\frac{R_0 + x}{R_0}\right), \\ r_{nl} = \frac{c^2}{\beta\omega_0 V_0}, \quad r_l = \frac{2c^3\rho}{b\omega_0}, \\ g(R) = \exp\left(\frac{R}{R_0}\right). \end{gathered} \tag{3}$$

Two important dimensionless parameters, which come in the definition of the inverse acoustic Reynolds number, $\mathrm{Re}_a^{-1} = \varepsilon = r_{nl}/r_{lin}$ are the characteristic distance over which the viscous dissipation effect becomes important, r_l and the characteristic distance over which nonlinear steepening of a planar wave develops leading to nonlinear wave interaction, r_{nl}. Furthermore, the physical meaning of R_0 parameter is to characterise how far the starting location of the acoustic wave emission (the effective source) is from the nonlinear wave interaction region. $\varepsilon g(R)$ plays the role of the effective viscosity coefficient, which in addition to the ratio of dissipation to inertia effects also contains the wave spreading factor $g(R)$ [31]. The latter factor appears because, in comparison with one-dimensional piston-like propagation of nonlinear waves, the energy of 3D waves is distributed over a spherical surface.

In the inviscid limit $\varepsilon \to 0$, the energy spectrum of random waves at very large distance has a universal behaviour at small frequencies [28,31], and the steepness $D = D(R)$ of the spectrum increases due to parametric generation of the low frequency components. In this case, the energy spectrum is given by

$$E(\omega, R) = D(R)\,\omega^2, \tag{4}$$

where

$$D(R) = R^{\frac{1}{2}} \ln^{-\frac{5}{4}}\left(\frac{R}{2\pi}\right) \simeq R^{\frac{1}{2}}. \tag{5}$$

Here, the standard definition for the energy spectrum is used

$$V(\omega, R) = F[V(t,R)] \equiv \frac{1}{2\pi}\int_{-\infty}^{\infty} V(t,R)\exp(-i\omega t)\,dt. \tag{6}$$

For stationary noise

$$< V(\omega, R) V^*(\omega', R) >= E(\omega, R)\delta(\omega - \omega') \tag{7}$$

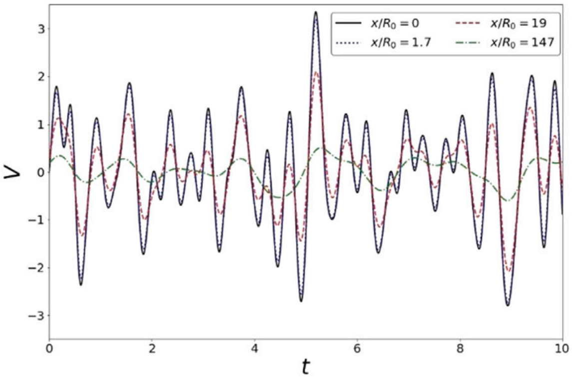

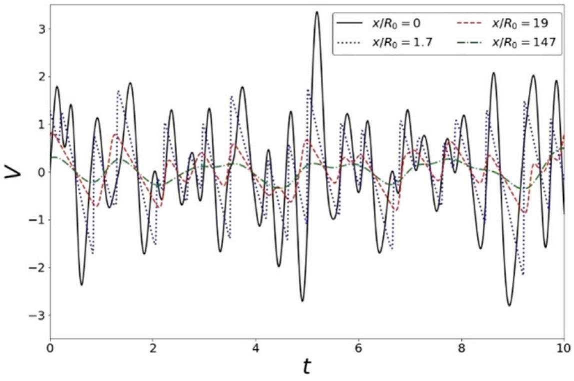

Fig. 1. Time domain solutions for the test problem of spherical wave propagation at acoustic Reynolds number $\mathrm{Re}_a = 100$ and different distances, x/R_0 from the source: linear propagation model (a) and nonlinear model (b).

where the triangular brackets denote statistical averaging, the asterisk is complex conjugation, and $\delta(x)$ is the delta function.

At very large distances from the source, when the acoustic energy generation at low frequencies is "arrested" by dissipation, the steepness $D = D_\infty\left(\varepsilon, R_0\right)$ no longer depends on the distance. The steepness value is determined by the processes of energy transfer to the low-frequency part of the spectrum during the nonlinear stage of the wave evolution. For the spherical wave, the asymptotic behaviour of the steepness factor is $D_\infty \approx \left(R_0 \ln(1/\varepsilon)\right)^{1/2}$ [31].

For finite distances from the emission location, no analytical solution is available, and the nonlinear wave propagation problem needs to be solved numerically. To illustrate the solution method and following [32], the governing Burgers' Eq. (2) and (3) is solved for parameters $R_0 = 1$ and $\varepsilon = 0.01$. The initial energy spectrum at the source location, x=0 is approximated by the Gaussian function,

$$E(\omega) = \frac{2}{\sqrt{\pi}}\omega^2 \exp\left(-\frac{\omega^2}{2}\right), \tag{8}$$

for which 100 realisations of the initial velocity signal are generated

$$V_0(\omega) = (A + iB)\sqrt{E(\omega)}, \tag{9}$$

where A and B are random Gaussian processes with zero mean and unit dispersion. Eq. (2) is solved in the spectral domain using the forward Euler integration scheme,

$$\begin{aligned} V(\omega, R + \Delta R) = V(\omega, R) + \frac{1}{2} i\omega F\left[\left(F^{-1}\left[V(\omega, R)\right]\right)^2\right]\Delta R \\ -\varepsilon \cdot \exp\left(\frac{R}{R_0}\right)\omega^2 V(\omega, R)\,\Delta R, \end{aligned} \tag{10}$$

where F and F^{-1} stand for the direct and inverse Fourier transforms, and the integration step, ΔR is selected to be sufficiently small for numerical accuracy.

Two propagation regimes are considered: (i) solution of the original nonlinear sound propagation problem and (ii) solution of the linear problem, which corresponds to artificially removing the quadratic velocity term from the right-hand-side of Eq. (10) in order to assess the nonlinearity effect on propagation. The frequency domain solution is converted to the time domain, and Fig. 1 compares instantaneous realisations of the nonlinear and linear wave propagation solution at different distances from the source. For the nonlinear model, steep wave fronts develop in the solution at $x = 1.7$. The coalescence of nonlinear waves leads to a notably faster decay of the wave-form amplitudes in comparison with the linear wave propagation.

For each distance from the source, the energy spectra are computed by ensemble averaging over the computed realisations. Results are presented in Fig. 2, which shows the spectra evolution of the nonlinear and linear propagation models as the distance from the source increases. For relatively small distances from the source, $x < 1$, which are within $r - r_0 < r_{nl}$, apart from high frequencies, the spectra are barely affected by the nonlinearity (Fig. 2(a) and Fig. 2(b)). At larger distances, which correspond to $1 < x < 100$, or $r_{nl} < r - r_0 < r_l$, the nonlinear wave interaction leads to a faster dissipation of the peak energy in comparison with the linear wave propagation regime. The transfer of energy to the high-frequency part of the spectra is also notable for the nonlinear propagation regime (Fig. 2(c)). For large distances, $x > 100$, or $r - r_0 > r_l$, when the dissipation mechanism becomes dominant for the most part of noise spectrum, the linear and nonlinear models converge to a similar solution (Fig. 2(d)).

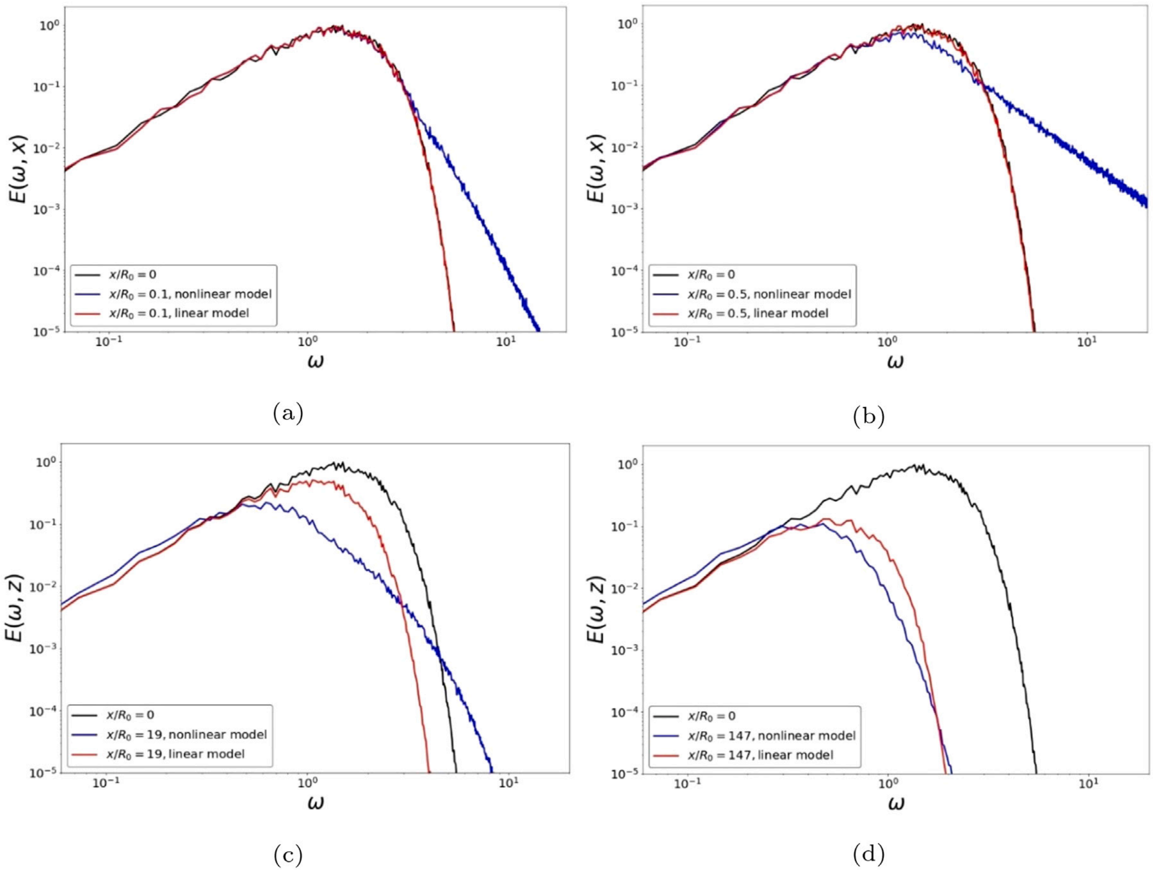

Fig. 2. Energy spectra for the test problem of spherical wave propagation at acoustic Reynolds number $\mathrm{Re}_a = 100$ and different distances x/R_0 from the source with and without including the nonlinearity effect: initial propagation, where the nonlinear wave interaction is not very important for the peak frequencies (a) and (b), strongly nonlinear wave interaction region (c), and the linear propagation stage dominated by viscous dissipation (d).

3. LTRAC jet case: summary of the text case, flow and acoustic near-field modelling

Following [25], the key details of the LTRAC jet flow simulation, corresponding conditions of the experiment conducted in the LTRAC Supersonic Jet Facility are summarised here. Compressed air is supplied to the plenum chamber at approximately $T_0 = 288$K, where high-resolution PIV measurements were taken. The nozzle is purely convergent with an inlet to exit area ratio of 93.44. It is axisymmetric with the diameter at the exit $D_j = 15$ mm and the nozzle lip thickness of 5 mm. The fully expanded flow conditions correspond to $M_{fe} = 1.59$, NPR=4.2, $D_{ef} = 16.73$ mm, $\mathrm{Re} = 1.06 \cdot 10^6$. The flow at the nozzle exit is sonic with a velocity of $U_j = 310$ m/s. A complete description of the facility and the PIV system can be found in [20].

For the LTRAC jet flow modelling, MILES are performed using the high-resolution CABARET method [33–35]. The CABARET properties include low dispersion and dissipation error as well as a compact computational stencil enabling an efficient implementation of the explicit asynchronous time stepping [36]. The computational domain starts downstream of the nozzle exit where characteristic boundary conditions are specified assuming the sonic condition, the same stagnation pressure as in the upstream chamber, and using the PIV data to impose the axial and radial velocity components. Downstream of the nozzle exit, three regions of local grid refinement are introduced, which includes the following zones: the jet plume, the region outside of the jet core, and the acoustic control surface region. An almost isotropic grid is generated using the OpenFOAM utility snappyHexMesh (sHM) in the jet shear layers and in the shock cell region. The total grid cell count is 70 million cells, and the grid size in the early shear layers is about 2% the nozzle exit diameter. The grid resolution in the acoustic surface region of the early shear layers corresponds to the maximum resolved Strouhal number (8 grid points per acoustic wavelength) of 2.6, and the same downstream of the end of the jet potential core is 1.7.

Thanks to the GPU implementation of the CABARET solver, a considerable reduction of the flow solution time is achieved in comparison with conventional LES approaches similar to the previous jet flow simulations [37–39]. The simulations are performed on a single computer workstation equipped with two GPU cards (NVidia Titan RTX 24 GB). The solution spin-out time is 300 convective time units (TUs), and a further 1000 TUs are simulated for statistical averaging. Here, 1 TU of the simulation corresponds to the

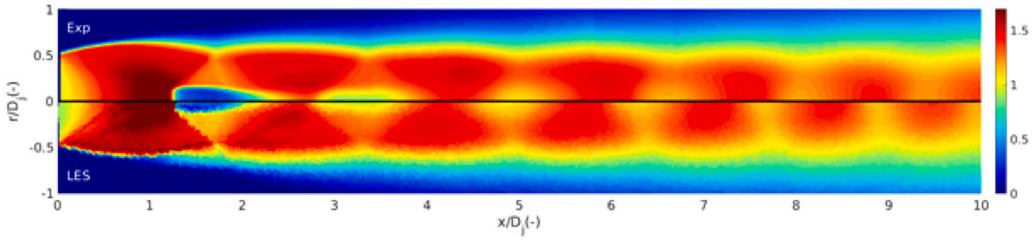

(a)

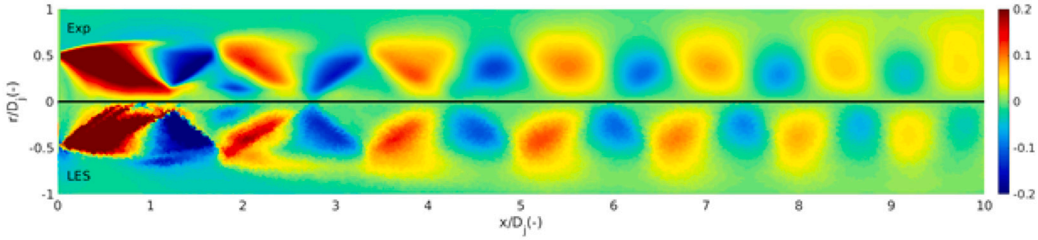

(b)

Fig. 3. Comparison of the LES solution (bottom half) with the PIV data (top half) for the axial (a) and radial (b) time-averaged velocity.

time taken by a turbulent eddy travelling at a speed equal to the jet velocity to cover the distance equal to one diameter of the nozzle exit. The total time to solution is 39 h.

Fig. 3 compares the distributions of the time-averaged axial and radial velocity components of the LES solution in the jet symmetry plane with the PIV data. And Fig. 4 shows similar comparisons for the root-means-square (r.m.s) of axial and radial velocity fluctuations. In all cases the normalisation of velocities and distances is performed based on D_j and U_j. Notably, the meanflow velocity distributions are in good agreement with the PIV data over the first 3-4 shock cells including the Mach disk, which are most important for BBSAN generation. Further downstream the phase error in the shock cell locations accumulates which suggests LES grid resolution being insufficient in this region.

Fig. 5 compares the centreline and lipline distributions of the time-averaged axial velocity from the LES solution with the PIV data. To illustrate the sensitivity of the LES solution to the grid, the results for the two LES resolutions 70 million and 24 million are shown. The 24 million grid is approximately twice coarser in terms of the grid density in the shear layer region in comparison with the 70 million mesh. Notably, both the LES solutions are in a good agreement with the experiment.

For turbulent velocity fluctuations, the LES solution shows some underprediction of turbulence in the initial shear layers and overprediction of turbulence intensity in the region of well-developed shear layers especially for the radial velocity fluctuations (Fig. 4). These discrepancies are believed to be related to the laminar inflow conditions at the nozzle exit and the LES grid that is of insufficient resolution to capture well both the time-averaged velocity and the turbulence. Notably, the LES solution captures reasonably well other salient features of the supersonic jet such as the multiple Prandtl–Meyer waves reflected from the jet shear layers and the centreline over 5-6 jet diameters downstream of the nozzle exit.

For acoustic near field noise calculations, the time-domain FW–H method is used with permeable acoustic integration surfaces including multiple closing discs [24]. In the method, the LES solution is recorded on a set of acoustic integration surfaces, which confine the turbulence, shock cells, and main vorticity regions in the jet shear layers (Fig. 6). The acoustic integration surfaces play the role of boundary conditions for the free-space Green's function method. The surfaces are of a funnel shape following the conically expanding jet shear layers. The funnel surface is terminated with a sufficient number of closing discs (16) at the outlet. By averaging the noise spectra predictions produced by each individual disc the pseudo-sound effects over a broad range of noise frequencies is avoided. The acoustic time signal is computed at the observer distance of $R/D_j = 20$ from the nozzle exit, which corresponds to the acoustic mid-field. The signal is converted to the power spectral density (PSD) based on the common definition and using Welch's averaging, such as used in [40]. In the previous work [25], it was shown that for all relevant frequencies the noise predictions of the LES-FW–H method are in 2-–3 dB agreement with the LTRAC acoustic measurements and the results of the NASA sJet model, which justifies the use of the FW–H method for the mid-range acoustic propagation modelling.

In the next section, the mid-field acoustic predictions of the LES-FW–H method will be used as a boundary condition (which equates to an initial condition for the space integration of the frequency domain problem) for long-range noise propagation governed by the spherical generalised Burgers' equation. The question to answer is whether the nonlinear wave-front steeping, which develops

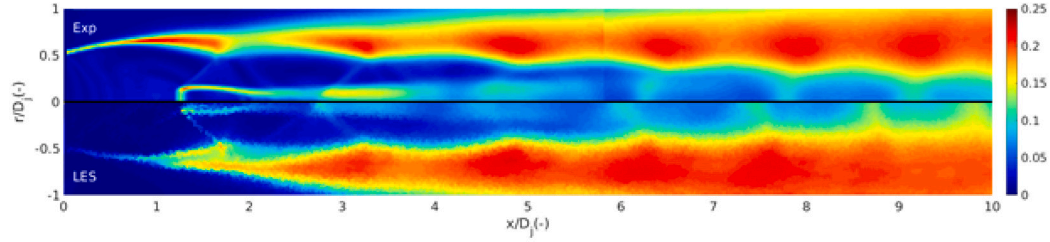

(a)

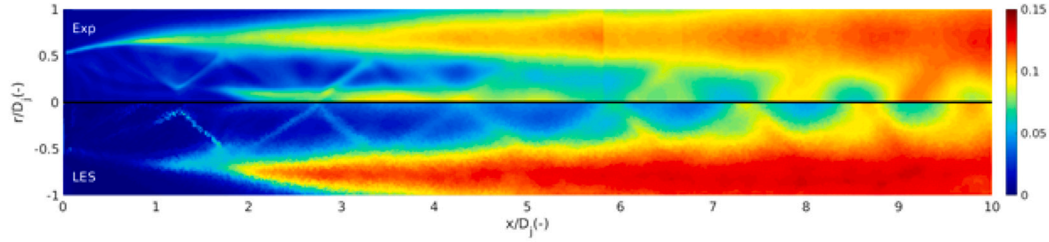

(b)

Fig. 4. Comparison of the LES solution (bottom half) with the PIV data (top half) for the axial (a) and radial (b) root-mean-square velocity fluctuations.

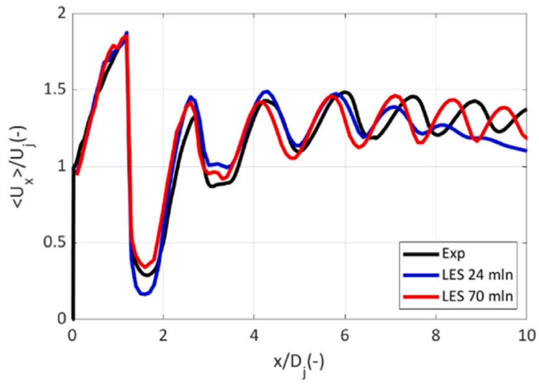

(a)

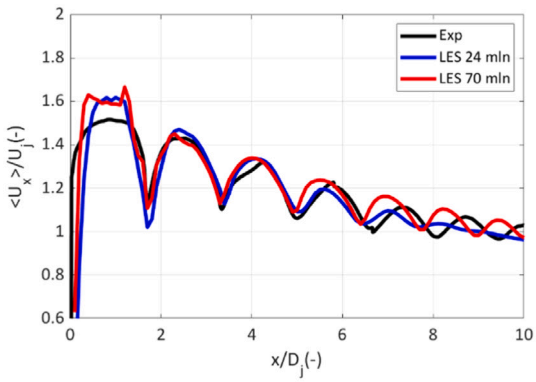

(b)

Fig. 5. Comparison of the axial time-averaged velocity profiles of the LES solutions on 70 and 24 million cells with the PIV data: (a) along the jet centreline and (b) along the jet lipline.

over long distances, plays a role for this LTRAC jet. The long-range propagation is defined by the distance when the noise frequencies around the peak of the noise spectra are completely attenuated by dissipation.

4. Far-field propagation of the supersonic jet noise

To specify the initial conditions for the Burgers' model in the frequency domain, the pressure spectra solution obtained from the FW–H method is converted to the acoustic velocity fluctuation with assuming a linear relationship between the amplitudes of pressure and velocity fluctuations, $u'(f) = p'(f)/\left(\rho_\infty c_\infty\right)$ in accordance with the linear acoustic wave model at $r/D_j = 20$. Two initial conditions of the spherical wave propagation are considered: the acoustic velocity spectra obtained from the LES-FW–H solution at 90° and 120° observer angle. These angles correspond to the region of peak directivity of BBSAN.

For both the conditions, the relevant sound wave propagation frequency is estimated from the peak BBSAN frequency, St = 0.4, which for the LTRAC jet is 13.12 kHz. The corresponding dimensionless parameters the Burgers' model Eq. (3) are summarised in Table 1.

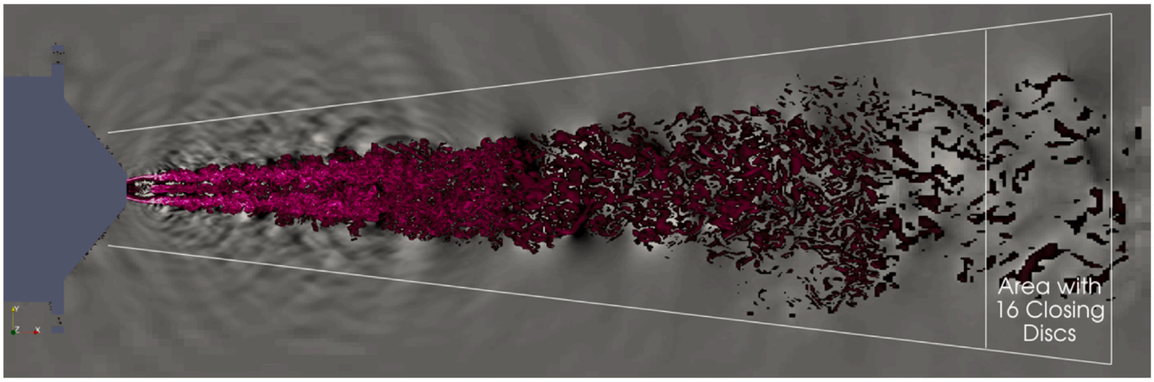

Fig. 6. LES solution for the LTRAC jet: instantaneous acoustic pressure field $\left(p - p_\infty\right) / p_\infty$ from −0.003 to 0.003 and contours of vorticity magnitude from 10000 to 500000 s^{-1}.

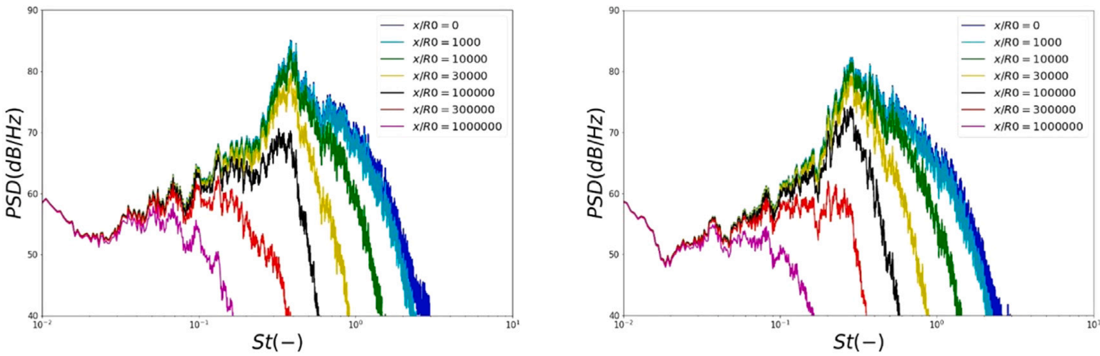

(a) (b)

Fig. 7. Generalised Burgers' solutions for the noise spectra of the LTRAC jet at different distances from the specified initial conditions corresponding to the LES-FW–H solution at (a) 90° and (b) 120° observer angles.

Table 1
Parameters of the Burgers' model of the LTRAC jet.

r_l	r_{nl}	ε	R_0
38841.34	7470	0.1923	$4 \cdot 10^{-5}$

Notably, the parameters correspond to the wave propagation regime, $R_0 \ll r_{nl} \ll r_l$, where the nonlinear effects are expected to start at much greater distances in comparison with the initial source radius. From this estimate, it may be expected that at a certain large distance from the source the solution of the Burgers' equation may reveal an interplay between the nonlinear wave steepening and viscous dissipation effects.

Having defined the initial spectrum of turbulent velocity fluctuations, 100 random realisations are generated using Eq. (9), and the discretised spherical Burgers' Eq. (10) is solved for each initial condition. The ensemble averaged spectra solutions are obtained for a range of propagation distances up to $x/R_0 = 10^6$, where the jet noise spectra are completely dissipated by viscosity for most frequencies. In jet units, this furthest distance corresponds to $1.8 \cdot 10^7$ initial jet diameters, which equates to 300 km from the nozzle exit. Fig. 7 shows the spectra solutions for the initial condition corresponding to 90° and 120° observer angles for several distances. For both the angles, the evolution of the acoustic spectra shows a similar behaviour: the high-frequency part of the spectra is gradually dissipated by viscosity while the low frequencies remain virtually unaffected. The local features of the original spectra including the narrow-band peak at St = 0.3 in the acoustic spectrum at 120° angle are well-preserved in the attenuated spectra shapes until very large distance, suggesting no apparent energy transfer between the low and high frequencies.

In order to quantify the effects of nonlinearity on far-field propagation of the LTRAC jet noise, the solutions of the generalised Burgers' equation for the same initial conditions are recomputed without the quadratic velocity term in Eq. (10). The comparison of the nonlinear and linear solutions of the Burgers' model for two typical distances from the source corresponding to the LES-FW–H noise spectra at 90° observer angle are shown in Fig. 8. The comparison for the initial condition corresponding to the other important BBSAN angle, 120° observer angle is very similar, hence, not included. The linear and nonlinear solutions perfectly coincide, which confirms that the effect of nonlinearity on the far-field noise propagation of the LTRAC jet is negligible.

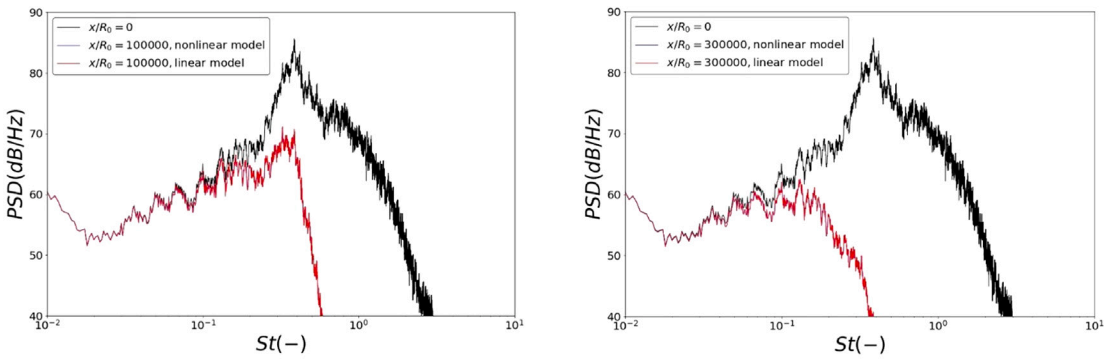

(a) (b)

Fig. 8. Comparison of the nonlinear and linear wave solutions of the generalised Burgers' equation for the noise spectra of the LTRAC jet using the LES-FW–H solution at 90° observer angle as initial condition for different distances from the source: (a) $x/R_0 = 10^5$ and (b) $x/R_0 = 3 \cdot 10^5$.

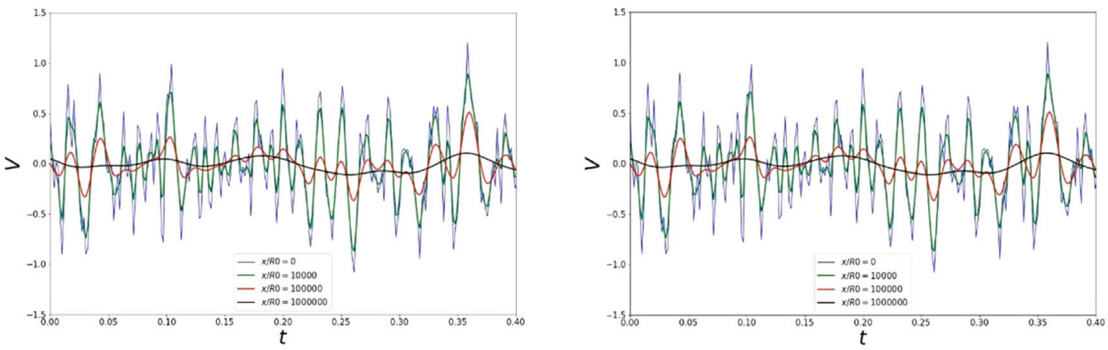

(a) (b)

Fig. 9. Comparison of the nonlinear and linear wave solutions of the generalised Burgers' equation for the noise spectra of the LTRAC jet using the LES-FW–H solution at 90° observer angle as initial condition for different distances from the source: (a) $x/R_0 = 10^5$ and (b) $x/R_0 = 3 \cdot 10^5$.

Finally, Fig. 9 shows the instantaneous velocity fluctuations (individual realisations of the stochastic solution) of the Burgers' model for the same initial condition as in Fig. 8. Again, the linear and nonlinear solutions are compared for several distances from the source. The nonlinear Burgers' solution virtually coincides with the linear one: the acoustic wave fronts do not exhibit any significant steepening at all times. Hence, for the considered LTRAC jet, the effects of the spherical pressure wave spreading dominates over the nonlinearity until the wave is attenuated by dissipation, thereby making the role of nonlinear wave propagation in shaping of the far-field noise spectra insignificant.

Finally, to further analyse the far-field propagation effects, we have performed an additional series of calculations of the cylindrical generalised Burgers' equation based on the same input from the LTRAC jet as for the spherical case. The cylindrical wave solution corresponds to a slower dissipation of high frequencies compared to the spherical waves. However, again, there is no appreciable difference between the linear and non-linear cylindrical wave propagation solutions. Hence, it is the low intensity of the considered laboratory jet case, which must be the reason for the relatively weak nonlinearity effect observed.

5. Conclusion

Noise generated by a supersonic under-expanded screeching jet, which has a strong Broad-Band-Associated-Noise (BBSAN) component and corresponds to a recent experiment in LTRAC (Laboratory for Turbulence Research in Aerospace and Combustion), is investigated using a triple-scale computational model. In the jet near-field, the Navier–Stokes equations are solved using the high-resolution CABARET method in the framework of the Monotonically Integrated Large Eddy Simulation approach, where the jet inflow condition at the nozzle exit is specified from the LTRAC Particle Image Velocimetry (PIV) data. The implementation of Graphics Processing Units (GPUs) with asynchronous time stepping allows solving the Navier–Stokes calculations on a locally refined grid of 70 Million cells on a single workstation computer equipped with several 'gaming' GPU cards within less than 2 days. The LES flow solution captures the shock cell structure and the Mach disk of the LTRAC jet in good agreement with the PIV data, and the agreement is reasonably insensitive to the grid resolution. The turbulent velocity fluctuations are less well resolved in the LES solution, however, important features of the supersonic jet such as multiple reflections of the Prandtl–Meyer waves in the jet core are well predicted by the LES, in agreement with the LTRAC experiment. The acoustic mid-field solution at the distance of 20 initial jet diameters from the nozzle exit is obtained by combining the LES solution with the Ffowcs Williams–Hawkings (FW–H) method based on the permeable control surface formulation. The mid-field solution is then used as a boundary condition for the spherical generalised Burgers' equation for long-range propagation using a numerical scheme in the frequency domain. The nonlinear and linear solutions of the Burgers' equation are compared for the same LES-FW–H dataset over a wide range of distances from the source, up to 18 million initial jet diameters. The results of the comparison show that the nonlinear wave propagation does not play any significant role in forming the characteristic hump in noise spectra typical of the nonlinear acoustic waves in this case. Hence, it is concluded that the case of the considered LTRAC jet falls under the category of small-scale supersonic jets. For such laboratory jets, in contrast to full-scale military or rocket jets, the nonlinear wave effects important in the jet near-field become completely negligible for the far-field acoustic wave propagation.

CRediT authorship contribution statement

S.A. Karabasov: Writing – original draft, Writing – review & editing, Conception and methodology. **A.P. Markesteijn:** Acquisition of data. **V. Gryazev:** Writing – original draft, Acquisition of data, Analysis and interpretation of data, Visualization. **A. Kalyan:** Writing – review & editing. **S.N. Gurbatov:** Writing – review & editing, Conception and methodology. **I.Yu. Demin:** Writing – review & editing, Conception and methodology. **A.A. Lisin:** Acquisition of data, Analysis and interpretation of data, Visualization. **A.V. Tyurina:** Acquisition of data, Analysis and interpretation of data, Visualization.

Declaration of competing interest

The authors declare that they have no known competing financial interests or personal relationships that could have appeared to influence the work reported in this paper.

Acknowledgements

The work is supported by the grants from the Russian Science Foundation: No. 19-12-00256. Sergey Karabasov acknowledges the study performed in TsAGI with the financial support provided by the Ministry of Science and Higher Education of the Russian Federation (Grant agreement of December 8, 2020 No 075-11-2020-023) within the program for the creation and development of the World-Class Research Center "Supersonic". The authors are grateful to Prof. Daniel Edgington-Mitchell and Dr Dominic Tan from Monash University for providing the PIV data of the LTRAC experiment.

References

[1] C.L. Morfey, G.P. Howell, Nonlinear propagation of aircraft noise in the atmosphere, AIAA J. 19 (8) (1981) 986–992, http://dx.doi.org/10.2514/3.51026.
[2] O.V. Rudenko, Interactions of intense noise waves, Sov. Phys. Uspekhi 29 (7) (1986) 620–641, http://dx.doi.org/10.1070/PU1986v029n07ABEH003460.
[3] K.L. Gee, T.B. Gabrielson, A.A. Atchley, V.W. Sparrow, Preliminary analysis of nonlinearity in military jet aircraft noise propagation, AIAA J. 43 (6) (2005) 1398–1401, http://dx.doi.org/10.2514/1.10155.
[4] R. Fiévet, C.E. Tinney, W.J. Baars, M.F. Hamilton, Coalescence in the sound field of a laboratory-scale supersonic jet, AIAA J. 54 (1) (2016) 254–265, http://dx.doi.org/10.2514/1.j054252.
[5] A.B. Vaughn, K.M. Leete, K.L. Gee, B.R. Adams, J.M. Downing, Evidence for nonlinear reflections in shock-containing noise near high-performance military aircraft, J. Acoust. Soc. Am. 149 (4) (2021) 2403–2414, http://dx.doi.org/10.1121/10.0003932.
[6] N. de Cacqueray, C. Bogey, Noise of an overexpanded mach 3.3 jet: Non-linear propagation effects and correlations with flow, Int. J. Aeroacoust. 13 (7–8) (2014) 607–632, http://dx.doi.org/10.1260/1475-472x.13.7-8.607.
[7] S. Saxena, P.J. Morris, K. Viswanathan, Algorithm for the nonlinear propagation of broadband jet noise, AIAA J. 47 (1) (2009) 186–194, http://dx.doi.org/10.2514/1.38122.
[8] M.R. Shepherd, K.L. Gee, M.S. Wochner, Short-range shock formation and coalescence in numerical simulation of broadband noise propagation, J. Acoust. Soc. Am. 126 (6) (2009) 2886–2893, http://dx.doi.org/10.1121/1.3243466.
[9] S.N. Gurbatov, O.V. Rudenko, Statistical phenomena, in: M. Hamilton, D. Blackstock (Eds.), Nonlinear Acoustics, vol. 13, Academic, San Diego, CA, 1998, pp. 377–398.
[10] O.V. Rudenko, Y.N. Makov, Sonic Boom: from the physics of nonlinear waves to acoustic ecology (a review), Acoust. Phys. 67 (1) (2021) 1–25, http://dx.doi.org/10.1134/S1063771021010036.
[11] W.J. Baars, C.E. Tinney, M.S. Wochner, M.F. Hamilton, On cumulative nonlinear acoustic waveform distortions from high-speed jets, J. Fluid Mech. 749 (2014) 331–366, http://dx.doi.org/10.1017/jfm.2014.228.
[12] J.E.F. Williams, J. Simson, V.J. Virchis, 'Crackle': an annoying component of jet noise, J. Fluid Mech. 71 (2) (1975) 251–271, http://dx.doi.org/10.1017/s0022112075002558.
[13] J. Lighthill, The inaugural theodorsen lecture, Theoret. Comput. Fluid Dyn. 6 (1994) 261–280.
[14] J.W. Nichols, S.K. Lele, F.E. Ham, S. Martens, J.T. Spyropoulos, Crackle noise in heated supersonic jets, J. Eng. Gas Turbines Power 135 (5) (2013) http://dx.doi.org/10.1115/1.4007867.
[15] P. Pineau, C. Bogey, Steepened mach waves near supersonic jets: study of azimuthal structure and generation process using conditional averages, J. Fluid Mech. 880 (2019) 594–619, http://dx.doi.org/10.1017/jfm.2019.729.
[16] M.F. Hamilton, Effective Gol'dberg number for diverging waves, J. Acoust. Soc. Am. 140 (6) (2016) 4419–4427, http://dx.doi.org/10.1121/1.4968787.
[17] K.L. Gee, V.W. Sparrow, M.M. James, J.M. Downing, C.M. Hobbs, T.B. Gabrielson, A.A. Atchley, The role of nonlinear effects in the propagation of noise from high-power jet aircraft, J. Acoust. Soc. Am. 123 (6) (2008) 4082–4093, http://dx.doi.org/10.1121/1.2903871.

[18] A. Langenais, F. Vuillot, J. Troyes, C. Bailly, Accurate simulation of the noise generated by a hot supersonic jet including turbulence tripping and nonlinear acoustic propagation, Phys. Fluids 31 (1) (2019) 016105, http://dx.doi.org/10.1063/1.5050905.

[19] P. Pineau, C. Bogey, Numerical investigation of wave steepening and shock coalescence near a cold Mach 3 jet, J. Acoust. Soc. Am. 149 (1) (2021) 357–370, http://dx.doi.org/10.1121/10.0003343.

[20] D. Edgington-Mitchell, K. Oberleithner, D.R. Honnery, J. Soria, Coherent structure and sound production in the helical mode of a screeching axisymmetric jet, J. Fluid Mech. 748 (2014) 822–847, http://dx.doi.org/10.1017/jfm.2014.173.

[21] D.J. Tan, D. Honnery, A. Kalyan, V. Gryazev, S.A. Karabasov, D. Edgington-Mitchell, Equivalent shock-associated noise source reconstruction of screeching underexpanded unheated round jets, AIAA J. 57 (3) (2019) 1200–1214, http://dx.doi.org/10.2514/1.j057400.

[22] D.J. Tan, D. Honnery, A. Kalyan, V. Gryazev, S.A. Karabasov, D. Edgington-Mitchell, Correlation analysis of high-resolution particle image velocimetry data of screeching jets, AIAA J. 57 (2) (2019) 735–748, http://dx.doi.org/10.2514/1.j057041.

[23] J.E.F. Williams, D. Hawkings, Sound generation by turbulence and surfaces in arbitrary motion, Philos. Trans. R. Soc. Lond. A 264 (1151) (1969) 321–342, http://dx.doi.org/10.1098/rsta.1969.0031.

[24] M.L. Shur, P.R. Spalart, M.K. Strelets, Noise prediction for increasingly complex jets. Part II: Applications, Int. J. Aeroacoust. 4 (3) (2005) 247–266, http://dx.doi.org/10.1260/1475472054771385.

[25] V. Gryazev, A. Kalyan, A.P. Markesteijn, S.A. Karabasov, Broadband shock-associated noise modelling for high-area-ratio under-expanded jets, J. Acoust. Soc. Am. 150 (2) (2021) 1534–1547, http://dx.doi.org/10.1121/10.0005976.

[26] A. Khavaran, J. Bridges, Development of jet noise power spectral laws using SHJAR data, in: 15th AIAA/CEAS Aeroacoustics Conference (30th AIAA Aeroacoustics Conference), American Institute of Aeronautics and Astronautics, 2009, http://dx.doi.org/10.2514/6.2009-3378.

[27] A. Khavaran, J. Bridges, SHJAR jet noise data and power spectral laws, NASA TM-2009-215608, 2009.

[28] S.N. Gurbatov, O.V. Rudenko, A.I. Saichev, Waves and structures in nonlinear nondispersive media, in: General Theory and Applications to Nonlinear Acoustics, vol. 472, Springer-Verlag and HEP, Germany, 2012, p. 500pp.

[29] S.N. Gurbatov, M. Deryabin, V. Kurin, D. Kasyanov, Evolution of intense narrowband noise beams, J. Sound Vib. 439 (2019) 208–218, http://dx.doi.org/10.1016/j.jsv.2018.09.042.

[30] V. Gryazev, A.P. Markesteijn, S.A. Karabasov, A. Kalyan, S.N. Gurbatov, I.Y. Demin, A. Lisin, When is nonlinear sound propagation important for broad band shock associated noise? in: AIAA AVIATION 2020 FORUM, American Institute of Aeronautics and Astronautics, 2020, http://dx.doi.org/10.2514/6.2020-2506.

[31] S.N. Gurbatov, I.Y. Demin, V.V. Cherepennikov, B.O. Enflo, Behavior of intense acoustic noise at large distances, Acoust. Phys. 53 (1) (2007) 48–63, http://dx.doi.org/10.1134/s106377100701006x.

[32] S.N. Gurbatov, O.V. Rudenko, A.V. Tyurina, Singularities and spectral asymptotics of a random nonlinear wave in a nondispersive system, Wave Motion 95 (2020) 102519, http://dx.doi.org/10.1016/j.wavemoti.2020.102519.

[33] V.M. Goloviznin, A.A. Samarskii, Finite difference approximation of convective transport equation with space splitting time derivative, J. Matem. Mod. 10 (1998) 86–100.

[34] S.A. Karabasov, V.M. Goloviznin, Compact accurately boundary-adjusting high-REsolution technique for fluid dynamics, J. Comput. Phys. 228 (19) (2009) 7426–7451, http://dx.doi.org/10.1016/j.jcp.2009.06.037.

[35] A. Chintagunta, S.E. Naghibi, S.A. Karabasov, Flux-corrected dispersion-improved CABARET schemes for linear and nonlinear wave propagation problems, Comput. & Fluids 169 (2018) 111–128, http://dx.doi.org/10.1016/j.compfluid.2017.08.018.

[36] V.A. Semiletov, S.A. Karabasov, CABARET scheme with conservation-flux asynchronous time-stepping for nonlinear aeroacoustics problems, J. Comput. Phys. 253 (2013) 157–165, http://dx.doi.org/10.1016/j.jcp.2013.07.008.

[37] A.P. Markesteijn, S.A. Karabasov, GPU CABARET solutions for the CoJen jet noise experiment, in: 2018 AIAA/CEAS Aeroacoustics Conference, American Institute of Aeronautics and Astronautics, 2018, http://dx.doi.org/10.2514/6.2018-3921.

[38] A.P. Markesteijn, S.A. Karabasov, CABARET solutions on graphics processing units for NASA jets: Grid sensitivity and unsteady inflow condition effect, C. R. Méc. 346 (10) (2018) 948–963, http://dx.doi.org/10.1016/j.crme.2018.07.004.

[39] A.P. Markesteijn, S.A. Karabasov, Simulations of co-axial jet flows on graphics processing units: the flow and noise analysis, Phil. Trans. R. Soc. A 377 (2159) (2019) 20190083, http://dx.doi.org/10.1098/rsta.2019.0083.

[40] V.A. Semiletov, S.A. Karabasov, A volume integral implementation of the goldstein generalised acoustic analogy for unsteady flow simulations, J. Fluid Mech. 853 (2018) 461–487, http://dx.doi.org/10.1017/jfm.2018.572.